Journal of Magnetic Resonance **157,** 235–241 (2002)
doi:10.1006/jmre.2002.2592

Laser-polarized ^{129}Xe NMR and MRI at Ultralow Magnetic Fields

Annjoe Wong-Foy,*,[1] Sunil Saxena,*,[2] Adam J. Moulé,* Hans-Marcus L. Bitter,* Juliette A. Seeley,* Robert McDermott,† John Clarke,† and Alexander Pines*,[3]

*Department of Chemistry, and †Department of Physics, University of California, Berkeley, and Materials Sciences Division, Lawrence Berkeley National Laboratory, Berkeley, California 94720

Received January 28, 2002; revised June 3, 2002

Laser-polarized ^{129}Xe and a high-T_c *s*uperconducting *qu*antum *i*nterference *d*evice (SQUID) are used to obtain magnetic resonance images in porous materials at a magnetic field of 2.3 mT, corresponding to a Larmor frequency of 27 kHz. Image resolution of 1 mm is obtained with gradients of only 1 mT/m. The resolution of xenon chemical shifts in different physicochemical environments at ultralow fields is also demonstrated. Details of the circulating flow optical pumping apparatus and the SQUID spectrometer are presented.

Key Words: **SQUID; imaging; laser polarized; xenon; ultralow field.**

INTRODUCTION

The practice of magnetic resonance imaging (MRI) currently necessitates powerful, homogeneous, and confining magnets that produce fields between ~0.5 and 10 T. MRI magnet design could be substantially simplified if the imaging were performed in ultralow magnetic fields approaching the Earth's magnetic field. At these fields, distortions due to spurious gradients produced by magnetic susceptibility variations over the sample are minimized (*1*). Furthermore, for a fixed relative homogeneity of the static field, the gradient strength required to achieve a given spatial resolution is decreased as the static field strength is decreased, owing to the reduction in the width of the intrinsic frequency distribution.

The difficulty of performing MRI at low fields is twofold: the nuclear spin polarization and the sensitivity of conventional (resonant circuit) magnetic resonance detectors both diminish linearly as the magnetic field strength is reduced, leading to a lower signal-to-noise ratio (SNR), ultimately the most important determinant of MRI information content. The first difficulty can be overcome by using optical pumping (*2–4*) to create an enhanced, nonequilibrium polarization of the nuclear spins to be imaged. The second difficulty can be addressed by detecting the NMR signal with a dc *s*uperconducting *qu*antum *i*nterference *d*evice (SQUID). We present ultralow field images of optically pumped samples detected using a SQUID.

The technique of optical pumping has considerably increased the utility of xenon for sensitive MRI of materials, gas flow, and living tissue at both high (*5–8*) and low (*1, 9–11*) fields. A major limitation of laser-polarized xenon MRI is the nonrenewable nature of the nuclear spin polarization: the completion of an MRI scan that uses a $\pi/2$ pulse destroys the polarization enhancement. Most laser-polarized xenon NMR and MRI methods employ the traditional batch pumping technique (*12–14*), which does not allow the use of multiple excitations with large tipping angles, e.g., for signal averaging or phase cycling. Here we describe an optical pumping approach, which removes these limitations by providing a continuous source of laser-polarized xenon. This optical pumping setup, based on similar methods used for high-field NMR (*15–18*), provides rapid optical pumping and delivery of xenon to the sample with retention of appreciable polarization during the passage of the xenon through magnetic field gradients.

The detector in our experiments is a high transition temperature (high-T_c) dc SQUID. The dc SQUID consists of a superconducting loop interrupted at two points by Josephson junctions. When properly biased with a static current, the SQUID acts as a magnetic flux-to-voltage transducer. As the SQUID measures magnetic flux directly, rather than the rate of change of flux (as is the case for a conventional tuned circuit detector), the SQUID detects NMR signals broadband at arbitrarily low frequencies without a loss in sensitivity (*19–21*). This frequency-independent response, coupled with unsurpassed field sensitivity, makes the SQUID far superior to the conventional tuned circuit for the detection of low-field NMR signals.

Using laser-polarized ^{129}Xe and SQUID detection we have performed spectroscopy and imaging experiments on room temperature samples in fields as low as 2 mT. An image of shaped aerogel using xenon, as well as images of xenon gas flow at ultralow fields, is presented. Finally, the resolution of chemical shifts of xenon in different physicochemical environments (*11*) at these low magnetic fields is demonstrated, hinting at the possibility for chemical-shift-selective imaging in ultralow fields.

[1] Current address: Bell Laboratories, Lucent Technologies, Murray Hill, NJ 07974. E-mail: wongfoy@lucent.com.

[2] Current address: Department of Chemistry, University of Pittsburgh, Pittsburgh, PA 15260. E-mail: sksaxena@pitt.edu.

[3] To whom correspondence should be addressed at Department of Chemistry, University of California, Berkeley, CA 94720. E-mail: pines@cchem.berkeley.edu.

1090-7807/02 $35.00

MATERIALS AND METHODS

Circulating Gas Flow Optical Pumping

Figure 1 shows a diagram of the optical pumping apparatus. The centerpiece is a Pyrex glass pumping cell (A). The reservoir (B) supplies rubidium vapor to the irradiation bulb (C) where it is excited by circularly polarized light at 794.7 nm from the laser (J). Collisions between the rubidium and the xenon atoms result in a transfer of polarization from the rubidium electrons to the xenon nuclei (*2–4*). The gas is then cooled in the water jacket (D) to condense out the rubidium vapor. Parts (B) and (C) are mounted inside an air-heated oven (not shown) made of aluminum with a 3.2-mm-thick quartz window. The oven is built into the center of a pair of 0.23-m-diameter Helmholtz coils (not shown), which produce a field of 8 mT. The xenon is circulated between the pumping cell and the sample by a sealed, high-pressure circulation pump (G), manufactured by Brey, Inc., which is capable of variable flow rates. Sitting on top of the fiberglass Dewar (F) used to control the temperature of the SQUID is the sample cell (E). The sample cell consists of a flat-bottomed, stoppered Pyrex glass cylinder with an inner diameter of 10 mm and capacity of about 1 ml with 6.4-mm Pyrex gas delivery tubes on opposite sides of the cell. The stopper provides easy access to the sample. All connections between components of the gas lines are made using Teflon PFA tubing and brass Swagelok fittings. Permanent brass ferrules are used for all brass to Teflon tubing connections, and Teflon ferrules serve for the brass to glass connections at the ends of the sample cell. The components are designed to hold a pressure of 10^6Pa. Finally, the solid-state diode laser (J), made by Opto-Power, Inc., provides a maximum continuous-wave power of 130 W at 795 nm. The light from the diode array is circularly polarized by a quarter-wave plate and then directed into the irradiation bulb of the pumping cell (C). Typically, 65 W of laser power were used for optical pumping.

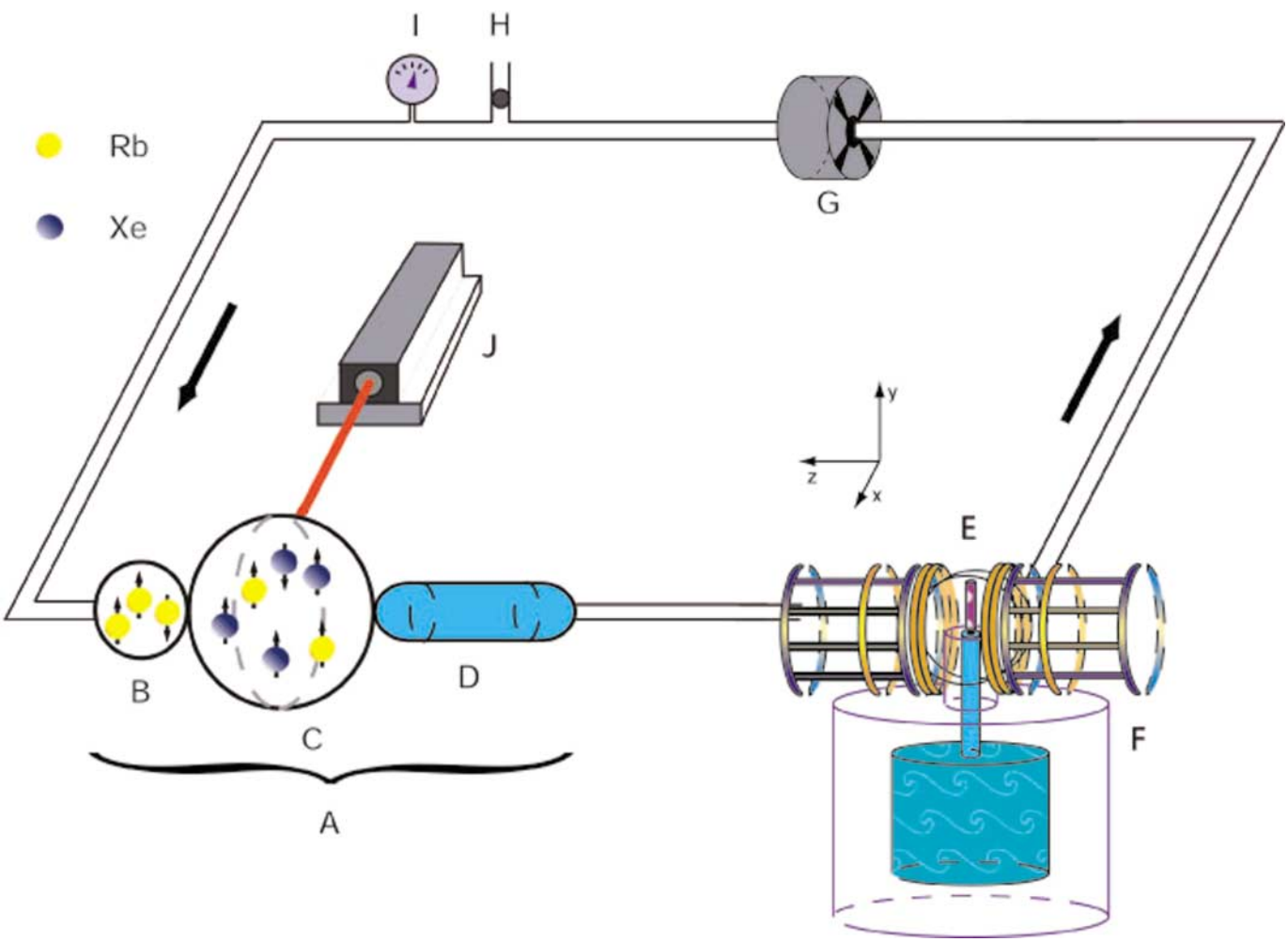

FIG. 1. Schematic of the circulating flow optical pumping apparatus. Natural abundance xenon is optically pumped in chamber (A), and then circulated to the SQUID MRI spectrometer using a gas circulation pump (G). The optical pumping chamber (A) consists of a rubidium reservoir (B), a main bulb (C) where circularly polarized light is directed from the laser (J), and a water condenser (D). The room temperature sample (E) sits 1.5 mm above the SQUID magnetometer. The magnetometer is contained within a liquid nitrogen Dewar (F), which cools the SQUID below its transition temperature.

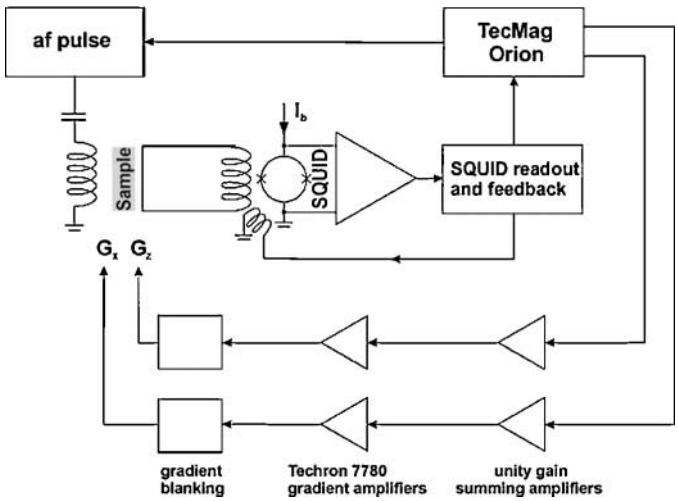

FIG. 2. Schematic of the SQUID spectrometer.

The gas mixture consists of $\sim 10^5$ Pa of natural abundance xenon, $\sim 10^5$ Pa of nitrogen gas for fluorescence quenching, and $\sim 5 \times 10^5$ Pa of helium for pressure broadening of the rubidium absorption line. The oven is heated to $\sim 143^\circ$C, providing a rubidium vapor pressure of 0.41 Pa, while the sample cell is maintained at room temperature. For the imaging experiments the gases were circulated at a constant flow rate of about 2.4×10^{-3} L/s.

SQUID MRI Spectrometer

The SQUID magnetometer consists of a square washer dc SQUID inductively coupled to a multilayer, 12-turn flux transformer in a "flip-chip" arrangement (*22*). Both the SQUID and the transformer were fabricated from thin films of the high-T_c superconductor $YBa_2Cu_3O_{7-x}$ patterned on $SrTiO_3$ substrates. The intrinsic noise of the magnetometer is 160 fT/Hz$^{1/2}$. Figure 1 (F) shows a schematic of the SQUID MRI hardware with coils while a circuit diagram of the MRI spectrometer appears in Fig. 2. The magnetometer is mounted in the vacuum space of a G10 fiberglass liquid nitrogen Dewar and is cooled below its superconducting transition temperature by a sapphire rod which is thermally anchored to the liquid nitrogen can (*23*). The sample, which is at atmospheric pressure and room temperature, is placed on a 76-μm-thick sapphire window positioned above the SQUID; the separation between the SQUID magnetometer and the sample is around 1.5 mm. In this configuration, the SQUID acts as an MRI surface coil, providing 2D projections along the y axis.

The static magnetic field is provided by a pair of Helmholtz coils, which produces a field of 2.26 mT per ampere of current. A second pair of Helmholtz coils, mounted orthogonally to both the magnetometer and the static coils, provides the excitation fields. Pulses are formed by a Hewlett Packard 3314A function generator, which is gated by TTL signals from a TecMag Orion console. The pulse current is amplified by 20 dB using a Krohn-Hite Model 3322 filter and fed into the excitation coils. This setup produces a maximum excitation field of 85 μT, yielding a $\pi/2$ time of 250 μs for xenon and 69 μs for protons.

For imaging experiments a pair of Maxwell coils and two sets of Golay coils are used to provide the gradients dB_z/dz, dB_z/dx, and dB_z/dy (Fig. 1). These are wrapped on a Lucite frame 0.35 m in length and 0.13 m in diameter. The static field and excitation coils fit inside this frame. The gradient coils are driven by Techron 7780 amplifiers, which are controlled by a TecMag DAC-18 gradient controller. Two modifications shown in Fig. 2 are required for optimum operation. First, the DAC-18 controller produces non-zero baseline voltages, which are amplified by the Techron 7780 amplifiers and result in significant currents—up to 100 mA—in the gradient coils. This is remedied by incorporating unity-gain summing amplifiers between the outputs of the DAC-18 controller and the inputs of the Techron 7780 amplifiers to adjust the offset voltages manually. Second, the current noise of the Techron amplifiers is sometimes as high as 10 mA. A blanking circuit is incorporated at the output of the amplifier to ground this excess current noise when the gradient pulses are turned off.

All imaging experiments are performed using the 2D "spin-warp" pulse sequence (*24*). The direct dimension consists of 4096 points collected with a dwell time of 12.5 μs. In the indirect dimension 32 phase-encoding gradient strengths are employed with the signal acquired at each strength averaged 400 times. Before 2-D Fourier transformation to produce the images, the indirect dimension is zero-filled to 128 points. The signal along the direct dimension is mixed down at the resonance frequency and digitally filtered to select a bandwidth of 2.5 kHz. No further apodization is applied in either dimension.

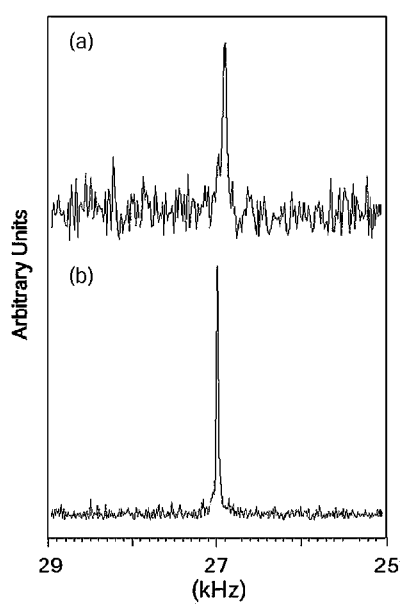

FIG. 3. (a) Proton and (b) xenon spectra obtained from 1-ml samples of mineral oil and laser-polarized xenon gas, respectively. The magnetic fields are 0.62 mT for protons and 2.3 mT for xenon, which corresponds to resonance frequencies of 27 kHz. The proton spectrum required 80,000 scans while the signal from laser-polarized xenon was obtained in 100 scans.

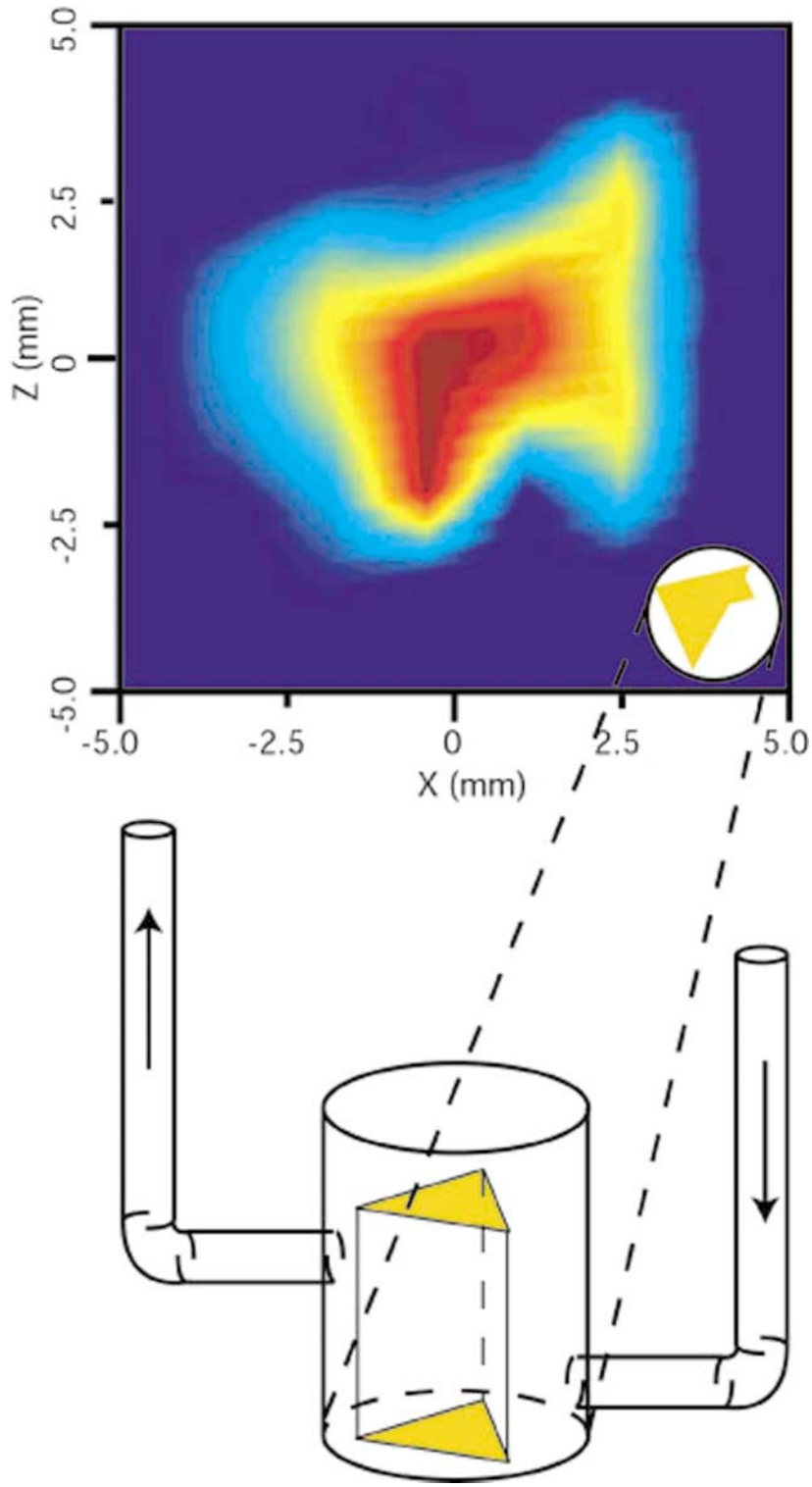

FIG. 4. MRI of xenon gas adsorbed on aerogel obtained at a magnetic field of 2.26 mT. A schematic of the sample cell is shown below the image. The MRI is a two-dimensional projection of the roughly triangular-shaped piece of aerogel (shown in the inset).

RESULTS AND DISCUSSION

Spin Polarization

Figure 3 compares the NMR signals from thermally polarized proton spins in mineral oil and from laser-polarized xenon spins produced in the continuous flow system. The static magnetic field is 0.62 mT for the proton and 2.26 mT for the xenon, so that the Larmor frequency is 27 kHz in both cases. This allows an easy and direct calibration of the xenon spin polarization. An SNR of ~3 is obtained from a 1-ml mineral oil (110 M in ^{1}H) sample after 80,000 scans. In contrast, the same volume of natural abundance hyperpolarized xenon gas at a pressure of 1 atm (0.01 M in ^{129}Xe) yields an SNR of ~30 after only 100 scans. This corresponds to a xenon spin polarization of ~1%, an enhancement of seven orders of magnitude over thermal spin

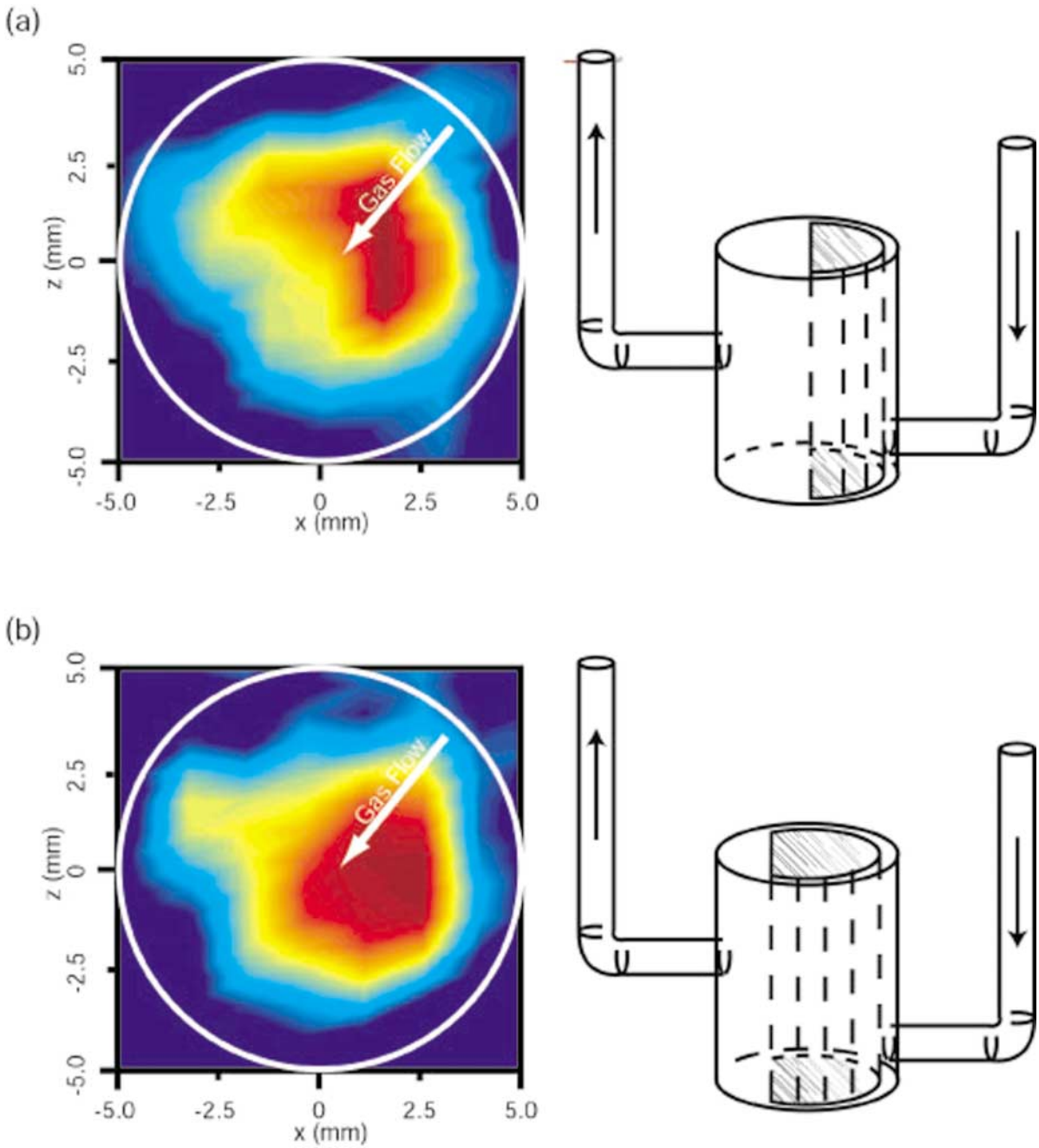

FIG. 5. Visualization of gas flow through a packed layer of aerogel. By varying the time between data acquisitions, the change in gas penetration into the aerogel can be directly observed. These measurements rely on the continuous xenon flow apparatus and the nonequilibrium nature of xenon laser polarization. a and b correspond to 0.5 and 2.0 s recycle delays, respectively. Insets are simple depictions of the polarized xenon in the aerogel at time t.

polarization at 2.26 mT. The flow and polarization of the ^{129}Xe spins in the continuous flow system maintain a constant signal over a period of at least 14 hours. This high-pressure, continuous flow pumping method generally yields lower xenon spin polarization than batch methods (which yield polarizations of tens of percent), but the advantages of "instant," renewable, and consistently polarized gas outweigh the reduced polarization. The decrease in polarization is explained in part by the fact that the flowing xenon gas is exposed to conditions that can rapidly degrade the spin polarization by relaxation, such as wall relaxation during flow, diffusion through magnetic field gradients, and high rubidium concentration in the pumping cell. Despite nonideal conditions, the polarizations are comparable to those achieved in similar setups used in high-field NMR (*15, 16*). Most importantly, the new continuous flow optical pumping system allows rapid signal averaging, which is necessary for the multiple-pulse NMR and MRI experiments described below.

Imaging

Figure 4 shows an image of laser-polarized xenon spins adsorbed in a roughly triangular piece of aerogel, a silicon-based, low-density, high-surface area solid foam. The image corresponds to a 2D projection parallel to the plane of the SQUID; a cross section of the piece of aerogel is shown in the inset. A schematic of the sample cell is shown below the image. The static field strength for this experiment was 2.26 mT, corresponding to a ^{129}Xe Larmor frequency of 26.7 kHz. The magnitude of the x gradient (direct dimension) was 1.1 mT/m giving a resolution of 1.4 mm. The maximum z gradient amplitude was 0.3 mT/m with a step size of 0.02 mT/m and pulse length of 42 ms. This indirect dimension has an intrinsic resolution of 2.9 mm and pixel resolution of 0.72 mm. The spatial resolution achieved is roughly an order of magnitude better than what one would achieve in a typical high-field *in vivo* imaging system with the same applied gradients, as in the high-field case the NMR lines are roughly an order of magnitude broader. The rounded corners in the image are partly due to limits of the resolution and possibly due to artifacts from nonlaminar gas flow around the object. Although the calculated Reynolds number is about 100, suggesting laminar gas flow, this estimate does not take into account the presence of aerogel in the flow path.

Figure 5 shows the direct visualization of xenon gas flow through aerogel. This quasi-stroboscopic imaging takes advantage of the gas flow system and the nonequilibrium nature of optical pumping. The sample cell, shown in the insets of Figs. 5a and 5b, is packed with crushed aerogel. At time $t = 0$, a $\pi/2$ pulse is applied to the sample to quench the longitudinal magnetization. After a time of t seconds, the spin-warp imaging pulse sequence is initiated and continued every t seconds. Under static conditions, there would be negligible signal since the xenon would relax to the thermal equilibrium polarization. However, since a continuous flow system is used, newly polarized xenon, which has entered the cell during each interval t, is detected. Thus, the effects of the flow of xenon during the time t can be observed. Images obtained with t of 0.5 and 2 s on the same sample are shown in Figs. 5a and 5b, respectively. Though the flow rates are identical in the two pictures, Fig. 5b shows deeper penetration of the polarized xenon into the aerogel sample compared to Fig. 5a due to the longer time that the newly polarized xenon is allowed to flow before imaging. Both images have a resolution of 1 mm in the x dimension and 0.7 mm in the z direction. They were collected using an x gradient strength of 0.8 mT/m and maximum z gradient amplitude of 0.3 mT/m with a step size of 0.02 mT/m and pulse length of 42 ms.

Spectroscopy

Figure 6 shows NMR spectra of hyperpolarized xenon flowing through powdered polypropylene, demonstrating the resolution of chemical shifts in ultralow fields (*11*). This system was chosen as the chemical shifts of ^{129}Xe adsorbed on polypropylene have been well characterized under a variety of conditions using high-field NMR (*25*). The 5-Hz upfield shift of the adsorbed

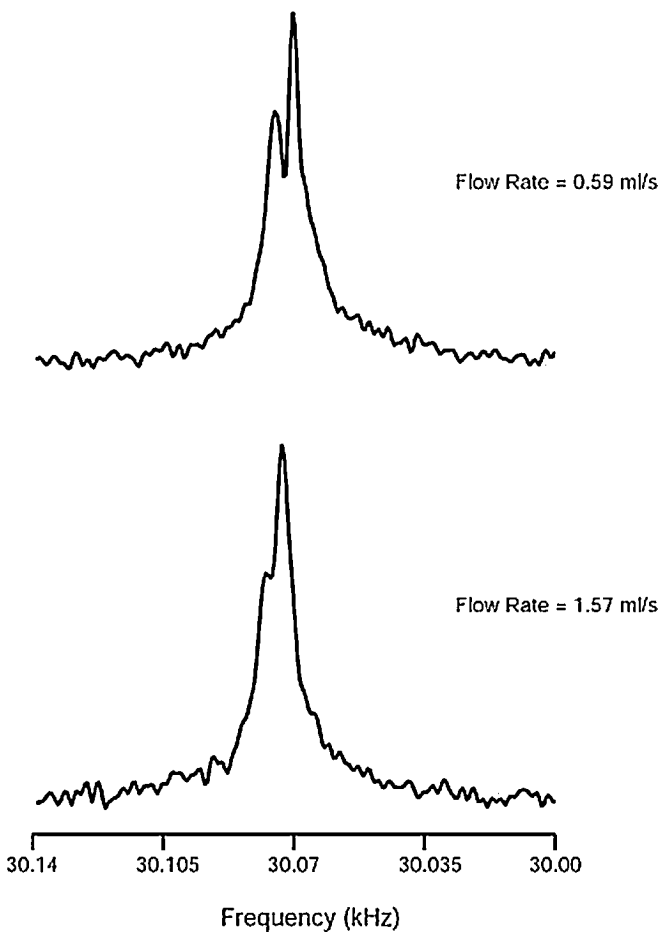

FIG. 6. NMR spectra of xenon flowing through polypropylene. At low flow rates (a), the chemical shift of xenon adsorbed to polypropylene is resolved from that of free xenon. Broadening due to flow and possibly exchange obscure the shift at a higher flow rate (b).

xenon in Fig. 6a corresponds to a 200 ppm chemical shift referenced to the gas peak at a Larmor frequency of 30.071 kHz. The line broadening arises from inhomogeneity of the static magnetic field and from gas flow with exchange between free and adsorbed xenon. As the flow rate increases, the lines become broader, obscuring the chemical-shift resolution as in Fig. 6b. To reduce this loss of resolution a stop-flow apparatus is being constructed such that the signal can be collected in the absence of gas flow. Further improvements include the design of more homogeneous magnets with shim coils. It is anticipated that with such modifications chemical shifts on the order of 10 ppm will be resolved, clearing the way for chemical-shift-selective imaging at ultralow fields. This result also suggests the feasibility of obtaining analytical information from NMR spectra and images acquired in the absence of high-field magnets.

SUMMARY

We have described a versatile ultralow field MRI spectrometer incorporating a circulating flow optical pumping system for ^{129}Xe. The circulating flow system provides a continuous source of xenon with a polarization $\sim$1%, a factor of 10^7 enhancement over thermal polarization at 2.3 mT. This is used in conjunction with sensitive SQUID detection to image materials with millimeter resolution. The gradients required to achieve this spatial resolution are at least an order of magnitude lower than those typically used in high-field MRI. A methodology for direct visualization of gas flows is described, and xenon chemical-shift resolution at ultralow fields has been achieved. These spin density images and chemical-shift measurements at 2.3 mT represent a step toward chemical-shift-selective imaging in low magnetic field.

ACKNOWLEDGMENTS

We thank Frank Ludwig for fabricating the multilayer $YBa_2Cu_3O_{7-x}$ flux transformer. This work was supported by the Director, Office of Science, Office of Basic Energy Sciences, Materials Sciences Division, of the U.S. Department of Energy under Contract No. DE-AC03-76SF00098.

REFERENCES

1. C. H. Tseng, G. P. Wong, V. R. Pomeroy, R. W. Mair, D. P. Hinton, D. Hoffmann, R. E. Stoner, F. W. Hersman, D. G. Cory, and R. L. Walsworth, *Phys. Rev. Lett.* **81,** 3785 (1998).
2. M. A. Bouchiat, T. R. Carver, and C. M. Varnum, *Phys. Rev. Lett.* **5,** 373 (1960).
3. B. C. Grover, *Phys. Rev. Lett.* **40,** 391 (1978).
4. W. Happer, E. Miron, S. Schaefer, D. Schreiber, W. A. van Wijngaarden, and X. Zeng, *Phys. Rev. A* **29,** 3092 (1984).
5. M. S. Albert, G. D. Cates, B. Driehuys, W. Happer, B. Saam, C. S. Springer, and A. Wishnia, *Nature* **370,** 199 (1994).
6. Y. Q. Song, H. C. Gaede, T. Pietrass, G. A. Barrall, G. C. Chingas, M. R. Ayers, and A. Pines, *J. Magn. Reson. A* **115,** 127 (1995).
7. G. Navon, Y. Q. Song, T. Room, S. Appelt, R. E. Taylor, and A. Pines, *Science* **271,** 1848 (1996).
8. E. Brunner, M. Haake, L. Kaiser, A. Pines, and J. A. Reimer, *J. Magn. Reson.* **138,** 155 (1999).
9. M. P. Augustine, A. Wong-Foy, J. L. Yarger, M. Tomaselli, D. M. TonThat, J. Clarke, and A. Pines, *Appl. Phys. Lett.* **72,** 1908 (1998).
10. M. Albert, A. Venkatesh, A. Zhang, C. H. Oh, F. Jolesz, L. Kubatina, and D. Balamore, 41st Exp. NMR Conf. in Asilomar, CA, 2000.
11. S. Saxena, A. Wong-Foy, A. J. Moulé, J. A. Seeley, R. McDermott, J. Clarke, and A. Pines, *J. Am. Chem. Soc.* **123,** 8133 (2001).
12. X. Zeng, Z. Wu, T. Call, E. Miro, D. Schreiber, and W. Happer, *Phys. Rev. A* **31,** 260 (1985).
13. D. Raftery, H. Long, T. Meersmann, P. J. Grandinetti, L. Reven, and A. Pines, *Phys. Rev. Lett.* **66,** 584 (1991).
14. Y. Q. Song, B. M. Goodson, and A. Pines, *Spectroscopy* **14,** 26 (1999).
15. B. Driehuys, G. D. Cates, E. Miron, K. Sauer, D. K. Walter, and W. Happer, *Appl. Phys. Lett.* **69,** 1668 (1996).
16. E. Brunner, R. Seydoux, M. Haake, A. Pines, and J. A. Reimer, *J. Magn. Reson.* **130,** 145 (1998).
17. R. Seydoux, A. Pines, M. Haake, and J. A. Reimer, *J. Phys. Chem. B* **103,** 4629 (1999).
18. L. G. Kaiser, T. Meersmann, J. W. Logan, and A. Pines, *Proc. Natl. Acad. Sci. USA* **97,** 2414 (2000).
19. R. C. Jaklevic, J. Lambe, A. H. Silver, and J. E. Mercereau, *Phys. Rev. Lett.* **12,** 159 (1964).
20. T. Van Duzer and C. W. Turner, "Principles of Superconductive Devices and Circuits," Elsevier North Holland, New York (1981).
21. J. Clarke, *in* "Superconducting Electronics" (H. Weinstock, Ed.), p. 1, NATO ASI Series No. 59 (1996).
22. F. Ludwig, E. Dantsker, D. Koelle, R. Kleiner, A. H. Miklich, D. T. Nemeth, J. Clarke, D. Drung, S. Knappe, and H. Koch, *IEEE Trans. Appl. Supercon.* **5,** 373 (1995).
23. T. S. Lee, E. Dantsker, and J. Clarke, *Rev. Sci. Instrum.* **67,** 4208 (1996).
24. P. T. Callaghan, "Principles of Nuclear Magnetic Resonance Microscopy," Oxford Univ. Press, London (1991).
25. H. W. Long, Ph.D. thesis, University of California, Berkeley (1993).